Magnetar field dynamics driven by chiral anomalies without magnetic helicity

Clara Dehman[1]*
[1] *Departament de Física, Universitat d'Alacant, 03690 Alicante, Spain*

The chiral magnetic effect (CME), arising from the chiral anomaly and enabling a mutual conversion between magnetic topology and fermionic chirality, is a key mechanism in magnetar field evolution. Previous work [1] demonstrated that the CME can efficiently generate dipolar fields ($B_{\rm dip} \gtrsim 10^{14}\,$G), consistent with magnetar timing measurements, provided that the initial magnetic field carries net helicity. However, whether neutron stars are born with magnetic helicity remains uncertain. In this work, we investigate the CME across a range of initial helicity configurations, including non-helical initial conditions. We find that the CME efficiently generates magnetar-strength dipoles on timescales of decades, independently of the initial helicity content. The instability is driven by localized helical structures that induce a residual chiral asymmetry and is primarily governed by the maximum chiral chemical potential, requiring $\mu_5^{\rm max} \gtrsim \text{few} \times 10^{-11}\,$MeV for onset in the magnetar regime. Our results further show that these dipoles may either remain stable and subsequently evolve through standard Ohmic decay, or become unstable if they acquire sufficient helicity, in which case they decay through the chiral anomaly, transferring energy to less helical modes. This outcome depends sensitively on the initial helicity distribution. These findings extend the applicability of the CME to more realistic magnetic-field configurations and underscore the importance of the helicity distribution at birth—a quantity that remains poorly constrained in neutron star formation, yet is crucial for determining neutron star magnetic evolution and magnetar formation.

I. INTRODUCTION

The transport of electric charge driven by quantum anomalies in chiral fermion systems has recently become a focal point of interest, particularly in the study of neutron stars and magnetars [1, 2]. This surge of attention reflects the possibility of accessing a distinct class of macroscopic quantum behavior that can directly influence the evolution of astrophysical magnetic fields. Conventional macroscopic quantum phenomena—such as superfluidity and superconductivity—emerge through symmetry breaking and are described by a local order parameter, for instance the Cooper-pair density [3]. By contrast, anomaly-induced effects in chiral systems originate from global topological properties and do not rely on symmetry breaking.

One of the most prominent manifestations of quantum anomalies is the chiral magnetic effect (CME), whereby a chirality imbalance among charged fermions induces an electric current parallel to an external magnetic field $\mathbf{B}$ via the Adler–Bell–Jackiw anomaly [4, 5]. The required chiral imbalance is tied, through the Atiyah–Singer index theorem [6], to the global topological structure of the gauge field. The CME provides a direct coupling between microscopic quantum anomalies and macroscopic magnetic-field evolution. In this framework, the induced current enters Maxwell's equations as a source term, so that a current aligned with the magnetic field twists magnetic flux and generates non-zero magnetic helicity. This coupling is reciprocal: magnetic helicity can in turn source chiral asymmetry as the field relaxes and untwists [1, 7], thereby establishing a feedback loop between fermionic chirality and magnetic topology.

The significance of this mechanism has long been questioned due to efficient, temperature-dependent chirality-flipping processes induced by finite fermion masses, in particular the electron mass in astrophysical plasmas, which tend to damp the chiral imbalance [8–10] and thereby limit its impact on magnetic-field evolution. While this suppression is effective in short-lived environments such as proto-neutron stars and the early Universe [9, 11], recent three-dimensional magneto-thermal simulations [1] show that, in long-lived neutron stars, the CME can still play a significant role even when such processes are fully taken into account. In particular, Dehman and Pons [1] showed that an initially small-scale, turbulent helical magnetic field[1] can, through the chiral anomaly, generate a residual chiral asymmetry between left- and right-handed electrons that persists for hundreds of years. This sustained asymmetry drives an inverse transfer of magnetic energy toward large scales, leading to the emergence of magnetar-strength dipolar components on timescales of order hundreds of years, without the need for an initial chiral imbalance.

This mechanism is especially relevant in the context of neutron stars, where the magnetic-field configuration at birth is expected to be dominated by small-scale structures. Magnetohydrodynamic (MHD) simulations indicate that the magnetic field is amplified during the proto-neutron star phase by a turbulent dynamo that can generate magnetar-level magnetic energies; however, most of this energy is stored in small-scale, non-axisymmetric,

* clara.dehman@ua.es

[1] A magnetic field configuration with non-zero magnetic helicity, reflecting a net global twist, writhe, or linkage of its field lines.

and predominantly toroidal components, leaving only a weak large-scale dipole [12–18]. Timing observations of magnetars—characterizing them as slow rotators—imply the presence of strong large-scale surface dipolar fields of order 10^{14} G. Three-dimensional long-term magneto-thermal evolution studies show that such initial magnetic field configurations cannot reproduce these properties when only Ohmic dissipation and Hall drift are considered [19–21], although they may be relevant for other neutron star classes, such as Central Compact Objects or low-field magnetars. This discrepancy suggests that an additional mechanism capable of transferring magnetic energy from small to large scales is required, making the CME a natural candidate.

However, the efficiency of the CME as a driver of inverse magnetic-energy transfer relies on the key assumption that the neutron star is born with an initially helical magnetic field [1]. The magnetic helicity content at birth remains largely unconstrained and may critically determine the efficiency of this mechanism. Whether newborn neutron stars carry a net helicity remains unclear, with theoretical arguments supporting both possibilities. Standard MHD simulations preserve reflection symmetry, so that an initially vanishing helicity leads to the development of mirror-symmetric structures with opposite handedness [22–24], allowing magnetic energy to grow while the net helicity remains negligible [25]. By contrast, net helicity may be generated if the CME operates during core-collapse supernovae: the initial chiral asymmetry is gradually erased as the system approaches chemical equilibrium, producing magnetic helicity through the anomaly [17]. However, this process is strongly suppressed by spin-flip reactions, which rapidly damp the chiral imbalance and may hinder the generation of net helicity.

Motivated by these uncertainties, we explore a range of magnetic field configurations representative of newborn neutron stars, systematically varying both the initial helicity content and its spatial distribution. Our goal is to identify which configurations can evolve into stable, large-scale dipolar fields characteristic of magnetars, and to assess whether the CME remains active when the initial magnetic field is non-helical, as may be expected at neutron star birth.

The structure of the paper is as follows. Section II introduces the theoretical framework employed in this work. Section III details the numerical setup and initial conditions. The results are presented in Section IV and discussed in Section V.

II. MAGNETIC FIELD FORMALISM

Magnetic helicity is a fundamental topological invariant, expressible in terms of the Chern–Simons three-form, and provides a quantitative measure of the twist, writhe, and linkage of magnetic-field lines [26–29]. It remains nearly conserved even in non-ideal, high–magnetic-Reynolds-number regimes, as demonstrated in studies of magnetic reconnection in the solar atmosphere [30], and is increasingly recognized as a key factor in neutron-star magnetic field evolution [1, 21, 31]. It is defined as

$$\chi_M = \int_V \boldsymbol{A}\cdot\boldsymbol{B}\, dV \tag{1}$$

where $\boldsymbol{A}$ is the magnetic vector potential, $\boldsymbol{B} = \boldsymbol{\nabla}\times\boldsymbol{A}$ is the magnetic field, and V denotes the integration volume.

The time evolution of χ_M is given by [32]

$$\frac{\partial(\boldsymbol{A}\cdot\boldsymbol{B})}{\partial t} \;=\; -2c\boldsymbol{E}\cdot\boldsymbol{B} - c\boldsymbol{\nabla}\cdot(\boldsymbol{E}\times\boldsymbol{A})\,, \tag{2}$$

where c is the speed of light and $\boldsymbol{E}$ the electric field. The term $\propto (\boldsymbol{E}\times\boldsymbol{A})$ represents the helicity flux across the boundary, whose contribution is negligible.

The same $\boldsymbol{E}\cdot\boldsymbol{B}$ term that governs helicity evolution in Eq. (2) also underlies the generation of chiral asymmetry through the chiral anomaly [33], linking electromagnetic fields to fermionic chirality and giving rise to the evolution equation for the chiral number density, $n_5 \equiv n_R - n_L$, [1, 4, 34]:

$$\frac{\partial n_5}{\partial t} = \frac{2\alpha}{\pi\hbar}\boldsymbol{E}\cdot\boldsymbol{B} - n_5\Gamma_f. \tag{3}$$

This equation contains both a source and a sink term. The $\boldsymbol{E}\cdot\boldsymbol{B}$ contribution can act as either, depending on its sign and thus on whether magnetic field lines are effectively twisted or untwisted. In contrast, the reaction rate Γ_f accounts for spin-flip interactions arising from electromagnetic effects and the finite electron mass; it always acts as a sink, reducing the efficiency of the CME and suppressing the chiral magnetic instability (CMI) [8–10, 34]. The magnitude of the spin-flip rate casts significant doubt on the relevance of the CME in short-lived environments such as proto-neutron stars and the early Universe [11]. Nonetheless, the first study of long-lived neutron stars [1] showed that chiral asymmetries can persist for centuries in the presence of small-scale, tangled magnetic fields, enabling a sustained transfer of magnetic energy from small to large scales despite strong suppression from spin-flip processes. For a simplified description of how the chiral anomaly operates, see Section II B.

Eq. (2) and Eq. (3), when combined and integrated over the volume, yield a generalized chiral–magnetic helicity balance law [1, 7, 33, 35]:

$$\frac{d}{dt}\left(Q_5 + \frac{\alpha}{\pi\hbar c}\chi_m\right) + \Gamma_5 = 0, \tag{4}$$

where $Q_5 = \int n_5\, dV$ is the total axial charge, quantifying the global imbalance between left- and right-handed fermions, and $\Gamma_5 = \int n_5\,\Gamma_f\, dV$ is the total spin-flip dissipation rate. The appearance of the sink term Γ_5 implies that this quantity is not strictly conserved.

The resulting local imbalance between left- and right-handed electrons induces an electric current parallel

to the magnetic field through the Adler–Bell–Jackiw anomaly [4, 5], giving rise to an additional term in Maxwell's equations [2, 36]:

$$\boldsymbol{J}_5 = \frac{\alpha\mu_5}{\pi\hbar}\boldsymbol{B}, \tag{5}$$

where $\mu_5 \equiv \mu_R - \mu_L$ is the chiral chemical potential, and $\alpha = e^2/(\hbar c)$ is the fine-structure constant, with e the elementary charge and $\hbar$ the reduced Planck constant. Gaussian units are used throughout this section.

In this work, we focus on the CME in the neutron star crust, where the spin-flip rate is given by $\Gamma_f = 4\alpha/(3\pi\sigma_e)$. This choice is motivated by our previous results showing that the CME can operate efficiently in the crust despite the presence of spin-flip processes [1]. In contrast, the neutron star core—which contains most of the stellar volume—is characterized by much stronger spin-flip damping, primarily due to electron scattering off magnetized neutron vortices in the superfluid [37, 38]. These processes occur on significantly shorter timescales than in the crust and are therefore expected to strongly suppress any chiral asymmetry. As a result, it remains unclear whether a residual chiral asymmetry could survive long enough to influence magnetic field evolution in the core, a question that warrants further investigation in future work.

Under these conditions, the magnetic field evolution in the crust is governed by the modified induction equation, which incorporates Ohmic dissipation, Hall drift, and the chiral magnetic contribution [1]:

$$\frac{\partial \boldsymbol{B}}{\partial t} = -\boldsymbol{\nabla}\times\left[\eta\left(\boldsymbol{\nabla}\times\boldsymbol{B} - k_5\boldsymbol{B}\right) + f_h\left(\boldsymbol{\nabla}\times\boldsymbol{B}\right)\times\boldsymbol{B}\right]. \tag{6}$$

The first term on the right-hand side represents Ohmic dissipation, where the magnetic diffusivity is defined as $\eta \equiv c^2/(4\pi\sigma_e)$, with σ_e denoting the electron conductivity. It leads to the decay of the magnetic field and is most effective at small spatial scales. The second term corresponds to the CME, with the chiral wavenumber defined as $k_5 = 4\alpha\mu_5/(\hbar c)$. This term can drive exponential growth of certain magnetic field modes by transferring energy from other modes. The last term represents the Hall drift, where $f_h = c/(4\pi e n_e)$ is the Hall prefactor, with n_e the electron number density. The Hall drift is known to generate a direct cascade, transferring magnetic energy from large-scale structures to smaller scales, where it is more efficiently dissipated by Ohmic diffusion [19, 39]. In addition, in the presence of helical (or partially helical) magnetic fields, it can also drive an inverse cascade [21, 31]. In this regime, the approximate conservation of magnetic helicity implies that, as magnetic energy is dissipated, the characteristic wavenumber shifts toward smaller values, corresponding to larger spatial scales. Consequently, the inverse cascade proceeds on the magnetic dissipation timescale. For a comprehensive overview of magneto-thermal evolution in neutron stars, we refer the reader to the recent review by Pons, Dehman, and Viganò [40].

A. Quasi-equilibrium and astrophysical timescales

When spin-flip reactions are included, their rates are extremely large—of order $10^{15} - 10^{17}$ s^{-1} under typical neutron-star conditions during the first few centuries. Because these rates exceed macroscopic magnetic-evolution timescales by many orders of magnitude, the system remains in a quasi-equilibrium state [see Section II of Ref. 1]. In this regime—effectively always realized in astrophysical contexts—one can derive an explicit expression for k_5 as a function of the magnetic field and its helicity density:

$$k_5 = \frac{k_{\boldsymbol{B}}}{1 + \left(\dfrac{2\mu_e^2}{m_e^2c^4}\right)\dfrac{B_{\rm QED}^2}{3\pi B^2}}, \tag{7}$$

where

$$k_B \equiv \frac{(\boldsymbol{\nabla}\times\boldsymbol{B})\cdot\boldsymbol{B}}{B^2}. \tag{8}$$

and $B_{\rm QED} \equiv m_e^2c^3/(e\,\hbar) = 4.41\times10^{13}$ G is the Schwinger critical field.

This expression shows that the chiral wavenumber k_5 is locally constrained by the characteristic wavenumber associated with currents aligned with the magnetic field, namely k_B. It also demonstrates that the CME operates efficiently only in the strong-field regime ($B \gtrsim B_{\rm QED}$), as realized in magnetars. This conclusion emerges naturally once spin-flip processes, often neglected in CME studies, are properly taken into account.

Neglecting the helicity flux across the boundaries, which is negligible in this context, Eq. (2) can be rewritten as

$$\frac{\partial(\boldsymbol{A}\cdot\boldsymbol{B})}{\partial t} = -2\,\eta\,(\boldsymbol{\nabla}\times\boldsymbol{B})\cdot\boldsymbol{B}\left(\frac{1}{1+\dfrac{B^2}{B_{sat}^2}}\right), \tag{9}$$

where $B_{\rm sat}$ is the characteristic magnetic field strength at which saturation sets in, given by

$$B_{\rm sat} \approx \sqrt{\frac{2}{3\pi}}\frac{\mu_e}{m_ec^2}B_{\rm QED}. \tag{10}$$

It scales linearly with the ratio $\mu_e/(m_ec^2)$, which increases with density, yielding $B_{\rm sat} \sim 10^{14}$ G near the surface and up to $\sim 5\times10^{15}$ G in deeper layers—consistent with inferred magnetar field strengths.

In the quasi-equilibrium limit, Eq. (9) links the evolution of magnetic helicity density to the current helicity density through the magnetic diffusivity. The sign and magnitude of $(\boldsymbol{\nabla}\times\boldsymbol{B})\cdot\boldsymbol{B}$ determine whether helicity is generated or dissipated. The efficiency of this process, and thus of the CME (see Eq. (4)), varies strongly with radius due to the steep diffusivity gradient. In regions with higher diffusivity, such as the outer crust and the nuclear pasta layer, magnetic structures relax more rapidly, facilitating a more efficient conversion between magnetic helicity and chiral asymmetry.

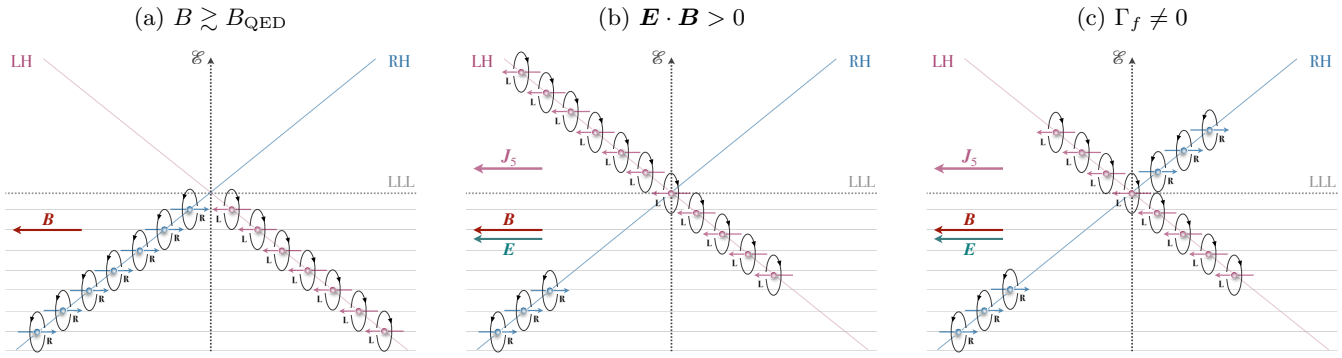

FIG. 1: Illustration of the chiral anomaly in a strong magnetic field regime, $B \gtrsim B_{\rm QED}$, oriented along the x-direction. Right-handed and left-handed electron momenta are shown in blue and pink, respectively. *Panel (a):* In the LLL, electrons can propagate only along the magnetic field. Right-handed electrons move opposite to $\boldsymbol{B}$, while left-handed electrons move along $\boldsymbol{B}$. Initially, equal populations of both chiralities are present. *Panel (b):* A non-vanishing $\boldsymbol{E}\cdot\boldsymbol{B}$ is induced as magnetic helicity relaxes. For $\boldsymbol{E}\cdot\boldsymbol{B} > 0$, right-handed electrons are converted into left-handed ones via momentum reversal, resulting in a net chiral asymmetry. The left-handed electron then moves upward. *Panel (c):* Excitation to higher Landau levels allows chirality-flipping processes, which relax the chiral imbalance on short timescales.

B. A simplified framework for the chiral anomaly

In ultra-strong magnetic fields exceeding the Schwinger QED critical value, $B_{\rm QED} \equiv m_e^2 c^3/(e\hbar) = 4.41 \times 10^{13}\,{\rm G}$, as expected in magnetar interiors, the motion of electrons perpendicular to the magnetic field is quantized into Landau levels, and only the lowest Landau level (LLL) is populated [41, 42]. Consequently, the transverse degrees of freedom are frozen, and in the LLL the electron spins anti-align with the magnetic field to minimize their energy, allowing electrons to propagate only along the field direction [43, 44]. If $\boldsymbol{B}$ points along the x-direction, negatively charged left-handed electrons propagate in the positive x-direction, while right-handed electrons propagate in the negative x-direction [45].

This effect is illustrated in panel (a) of Figure 1, where the magnetic field is assumed to be uniform and oriented along the x-direction, i.e., $\boldsymbol{B} = B_x\hat{\boldsymbol{x}}$. Initially, equal numbers of left-handed and right-handed electrons are present, corresponding to neutron-star matter in chemical equilibrium, with no net chiral asymmetry.

As the magnetic field lines locally untwist, the magnetic helicity decreases slightly due to finite magnetic diffusivity, inducing a locally positive $\boldsymbol{E}\cdot\boldsymbol{B}$ term. In this case, some electrons undergo helicity flips. Since spin flips are energetically suppressed in a strong magnetic field, helicity can only change via a reversal of the electron momentum. For $\boldsymbol{E}\cdot\boldsymbol{B} > 0$, the induced electric field is locally aligned with the magnetic field: left-handed electrons moving along the field propagate upward, while right-handed electrons are converted into left-handed electrons through a reversal of their momentum [45]. Although the total electron number, $N_e = N_R + N_L$, is conserved, the axial charge, N_5, is not, leading to the generation of an axial current, $\boldsymbol{J}_5$, along the direction of $\boldsymbol{B}$, which reflects the presence of the chiral (axial) anomaly. In this scenario, the evolution of the magnetic field couples primarily to the left-handed current, $\boldsymbol{J}_5 \simeq \boldsymbol{J}_L$. This mechanism is illustrated in panel (b) of Figure 1.

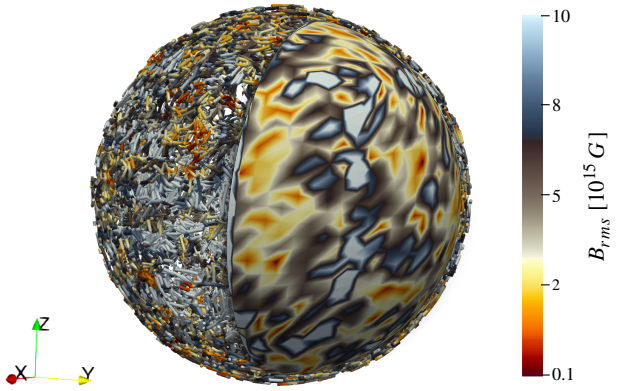

FIG. 2: Schematic representation of the initial small-scale tangled magnetic field configuration.

In addition to the anomalous generation of axial charge by a non-vanishing $\boldsymbol{E}\cdot\boldsymbol{B}$, chirality-flipping processes act to relax the resulting imbalance [8]. In the ultra-strong magnetic-field regime, where electrons predominantly occupy the LLL, genuine spin-flip interactions cannot occur within the LLL, which admits only a single spin polarization [44]. Such processes therefore become effective only when electrons are excited to higher Landau levels, where spin and momentum are no longer rigidly locked and chirality is not conserved [46]. Finite electron-mass

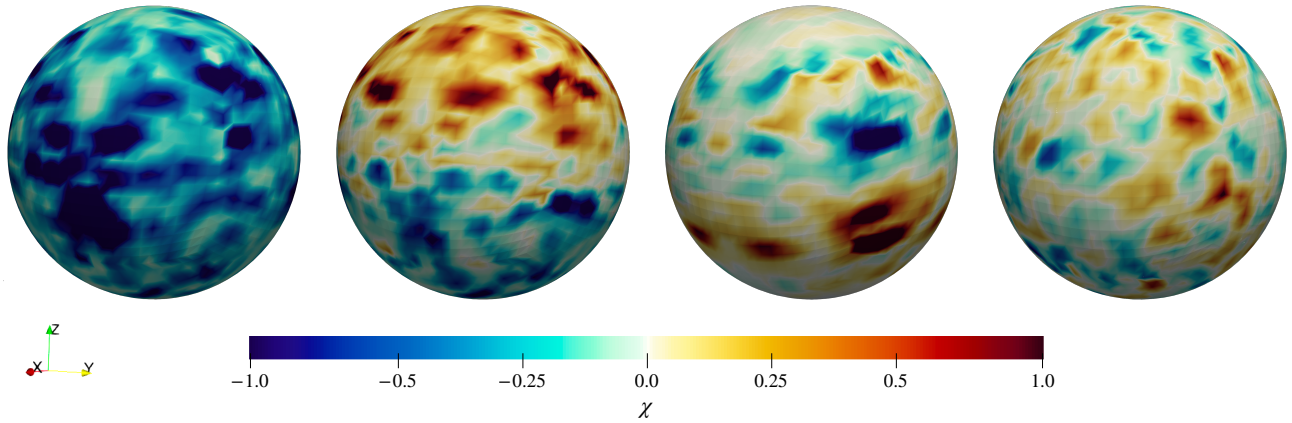

FIG. 3: Schematic representation of the initial local magnetic helicity χ, normalized by its maximum absolute value, for the `Monohel`, `Bihel`, `Mixhel`, and `Angfluc` setups, from left to right.

effects and electromagnetic scattering processes then convert right- and left-handed electrons into one another, leading to a relaxation of the axial charge N_5. The role of these chirality-flipping processes is illustrated in panel (c) of Figure 1. These processes occur on very short timescales and can therefore be regarded as effectively instantaneous and local within the interior of a neutron star.

It is important to note that an electric field anti-aligned with the magnetic field ($\boldsymbol{E}\cdot\boldsymbol{B} < 0$) corresponds to a system with an initial chiral asymmetry, which is converted into magnetic helicity via the chiral anomaly relation (see Eq. 2). Such a scenario is expected, for instance, in proto-neutron stars, where weak interactions couple preferentially to left-handed electrons, giving rise to a chiral imbalance. As the neutron star forms, the system evolves toward chemical equilibrium and the populations of left- and right-handed electrons become comparable. During this evolution, the system exhibits $\boldsymbol{E}\cdot\boldsymbol{B} < 0$, leading to the conversion of left-handed electrons into right-handed ones. This evolution corresponds to a transition from panel (b) to panel (a) in Figure 1.

III. NUMERICAL SETUP

To study the magnetic field evolution under the CME, we use the extended `MATINS` code introduced in Dehman and Pons [1], which, in addition to solving the coupled induction and heat-diffusion equations, self-consistently incorporates the evolution of the chiral number density and spin-flip processes arising from the chiral anomaly. This extension builds on the earlier version of `MATINS`[2] described in Dehman *et al.* [19, 47], Ascenzi *et al.* [48], which did not include the CME.

We model the entire neutron star volume but restrict magnetic field evolution to the crust by imposing potential-field (current-free) boundary conditions at a mass density of $\rho = 10^{10}\,\mathrm{g\,cm^{-3}}$, which defines the numerical surface of the star, and perfect-conductor conditions at the crust–core interface, thereby confining the magnetic field to the crust (see Dehman *et al.* [47] for details on the magnetic boundary conditions). The temperature-dependent electrical conductivity is computed using the IOFFE codes[3] [49]. The stellar background in `MATINS` is constructed using zero-temperature equations of state (EOSs) from the CompOSE[4] database. In this work, we adopt the BSk24 EOS [50] and consider a canonical $1.4\,M_\odot$ neutron star, yielding $R = 12.4\,\mathrm{km}$ and a crust thickness of 0.86 km, although `MATINS` allows exploration of alternative EOSs and stellar masses.

The magnetic field configuration of neutron stars at birth remains poorly constrained, and consequently both its helicity content and spatial distribution are largely unknown. During the proto-neutron star stage, dynamo processes are expected to drive the system toward a quasi-equilibrium state in which magnetic energy is distributed across a broad range of spatial scales. This configuration is typically dominated by non-axisymmetric and toroidal components, with only a weak large-scale dipolar field [12–15, 18, 51]. While the total magnetic energy can reach magnetar-like values, it is predominantly concentrated on small spatial scales.

Rather than attempting to model the full diversity of magnetic-field configurations predicted by proto-neutron-star studies, we initialize the system with a magnetic field whose energy is concentrated at small spatial scales and whose spectrum peaks at a characteristic angular wavenumber ℓ_0. In the sub-inertial range ($\ell < \ell_0$),

[2] https://github.com/ice-csic-astroexotic/MATINS

[3] http://www.ioffe.ru/astro/conduct/

[4] https://compose.obspm.fr/

TABLE I: Simulation data at different representative times, showing the magnetic field strength (mean and dipolar components), the chiral chemical potential (mean and maximum values), and the dimensionless fractional helicity, $\tilde{\chi}$.

Run	$B_{\rm rms}$ [G]		$B_{\rm dip}$ [G]		$\mu_5^{\rm avg}$ [MeV]		$\mu_5^{\rm max}$ [MeV]		$\tilde{\chi}$	
	$t=0$	100 yr	$t=0$	100 yr	$t=0$	100 yr	$t=0$	100 yr	$t=0$	1000 yr
`Monohel`	2.9×10^{16}	2.3×10^{16}	4.3×10^{12}	1.0×10^{14}	2×10^{-12}	1×10^{-12}	2×10^{-11}	1×10^{-11}	4×10^{-6}	$0.7\,\tilde{\chi}^{t0}_{\rm Mo}$
`Bihel`	3.0×10^{16}	2.0×10^{16}	4.1×10^{12}	1.6×10^{14}	-5×10^{-14}	-5×10^{-14}	8×10^{-11}	2×10^{-11}	$3.5\%\,\tilde{\chi}^{t0}_{\rm Mo}$	$1.7\,\tilde{\chi}^{t0}_{\rm Bi}$
`Mixhel`	3.1×10^{16}	1.8×10^{16}	4.0×10^{12}	1.4×10^{14}	-2×10^{-13}	-1×10^{-13}	9×10^{-11}	2×10^{-11}	$10\%\,\tilde{\chi}^{t0}_{\rm Mo}$	$1.6\,\tilde{\chi}^{t0}_{\rm Mi}$
`Angfluc`	2.8×10^{16}	1.5×10^{16}	4.3×10^{12}	1.5×10^{14}	9×10^{-15}	2×10^{-14}	1×10^{-10}	2×10^{-11}	$0.9\%\,\tilde{\chi}^{t0}_{\rm Mo}$	$5.3\,\tilde{\chi}^{t0}_{\rm Ag}$
`Radfluc`	2.8×10^{16}	1.3×10^{16}	4.0×10^{12}	1.1×10^{14}	-3×10^{-15}	-2×10^{-15}	9×10^{-11}	2×10^{-11}	$0.2\%\,\tilde{\chi}^{t0}_{\rm Mo}$	$7.5\,\tilde{\chi}^{t0}_{\rm Rd}$

we adopt a spectrum corresponding to a random vector potential. In three dimensions, this implies a vector potential spectrum $E_A(\ell) \propto \ell^2$ and a magnetic energy spectrum $E_M(\ell) \propto \ell^4$ (see Table 1 of Dehman and Brandenburg [21]). This form, commonly used in cosmology and referred to as a causal spectrum [52], describes a divergence-free field with no spatial correlations beyond the generation scale. The magnetic energy spectrum peaks at $\ell_0 \simeq 50$ and extends up to $\ell_{\rm max} = 70$.

For the radial wavenumber k_r, we adopt values of order a few hundred, chosen to balance the fastest-growing mode of the CMI against Ohmic dissipation (see Appendix II of Dehman and Pons [1]). The radial direction is resolved more finely than the angular directions for both physical and numerical reasons. Physically, the CME is sensitive to neutron-star microphysics, which exhibits strong radial gradients. Numerically, `MATINS` is not parallelized, and the spherical harmonic decomposition required for higher angular resolution is computationally demanding. Accordingly, the crust is discretized with 200 radial grid points, allowing structures down to scales of tens of meters to be resolved. The angular directions are discretized using a cubed-sphere grid [47] with $N_\xi = N_\eta = 47$ points per patch over six patches, corresponding to effective resolutions of $N_\theta = 94$ and $N_\varphi = 188$, and resolving angular scales of several hundred meters.

With this numerical setup, the initial magnetic field has a characteristic strength of order 10^{16} G, predominantly concentrated at small scales and close to equipartition between poloidal and toroidal components, with a slight dominance of the toroidal component. The large-scale dipolar field is limited to $\sim 10^{12}$ G, yielding a total magnetic energy of $\sim 10^{49}$ erg, consistent with expectations for neutron-star birth [15, 16]. An example of such an initial configuration is shown in Figure 2, where the color scale indicates the magnetic field strength.

Since the magnetic helicity at neutron-star birth remains largely unconstrained, we explore several initial configurations spanning plausible scenarios for a newborn neutron star. This allows us to assess whether an initially non-helical magnetic field can transfer magnetic energy across scales and lead to large-scale field formation. The helicity distributions considered in this study are listed below:

(i) `Monohel` – a helical configuration with uniform helicity sign throughout the crust;

(ii) `Bihel` – a bi-helical configuration with opposite helicity signs in the northern and southern hemispheres, yielding an approximately vanishing net helicity;

(iii) `Mixhel` – a configuration with mixed helicity across hemispheres, also yielding an approximately vanishing net helicity;

(iv) `Angfluc` – a configuration with small-scale angular helicity fluctuations, leading to an approximately vanishing net helicity;

(v) `Radfluc` – a configuration with small-scale radial helicity fluctuations, also yielding an approximately vanishing net helicity. In this case, different radial functions are used for the poloidal and toroidal components.

(vi) `NoCME` – identical to the `Bihel` setup but with the CME deactivated, serving as a reference case.

Details on the construction of each configuration are provided in Appendix A, and the key parameters are summarized in Table I. The local three-dimensional distribution of the initial magnetic helicity, normalized by its maximum absolute value, $\chi(r,\xi,\eta,t) = \boldsymbol{A}\cdot\boldsymbol{B}/\left|\boldsymbol{A}\cdot\boldsymbol{B}\right|_{\rm max}$, is shown in Figure 3 for the `Monohel`, `Bihel`, `Mixhel`, and `Angfluc` runs. For the `Radfluc` run, see Figure 9 in Appendix A. This normalization is used to visualize the spatial distribution of positive and negative helicity regions and to enable comparison across simulations. It does not provide a measure of the global helicity content. Note that values of ±1 in χ correspond to the local extrema of the normalized helicity density and do not imply a fully helical magnetic field configuration, since χ is normalized by its maximum absolute value. A quantitative assessment of the helicity content in each configuration is discussed in the next section.

Each setup is evolved in full crustal simulations over the first thousand years using day-long timesteps. We focus on these early stages to assess whether the CME can contribute to the formation of young magnetars such as Swift J1818.0–1607 (~ 200 yr; 53) on such short

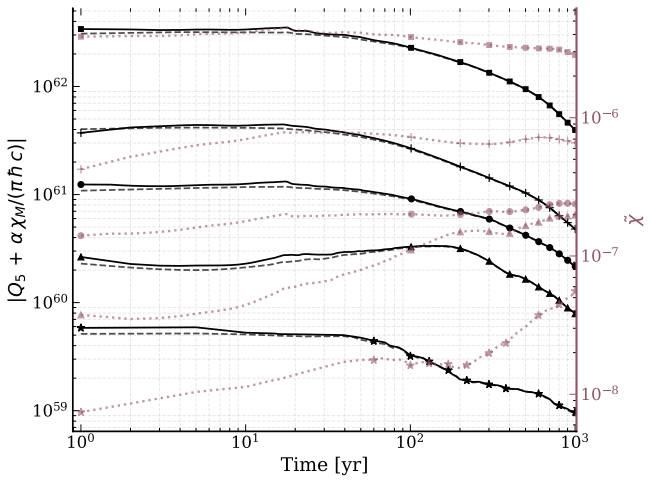

FIG. 4: Evolution of helicity-related quantities. The left y-axis shows the generalized helicity (Eq. 4), $|Q_5 + \frac{\alpha}{\pi\,\hbar\,c}\,\chi_M|$ (solid lines), together with the losses due to the spin-flip term, $|\Gamma_5\,\Delta t|$ (dashed lines). The right y-axis shows the dimensionless fractional helicity, $\tilde{\chi}$ (dots). Different simulation runs are distinguished by markers: squares (`Monohel`), circles (`Bihel`), plus signs (`Mixhel`), triangles (`Angfluc`), and stars (`Radfluc`).

timescales. To isolate CME effects from those of the Hall drift—which also redistributes magnetic energy across scales—we switch off the Hall term in this study. The role of Hall evolution is discussed at the end of Section IV.

IV. RESULTS

A. Helicity analysis

The conservation of generalized helicity (Eq. 4) and its numerical verification are presented in Figure 4 (left y-axis; black). The solid lines show the time evolution of the total helicity, $|Q_5 + \frac{\alpha}{\pi\,\hbar\,c}\,\chi_M|$, while the dashed lines represent the losses due to spin-flip processes at each time step, $|\Gamma_5\,\Delta t|$. This term quantifies the net reduction of chiral charge associated with electron chirality-flipping interactions integrated over the crust over a single time step. Different simulation runs are distinguished by markers: squares (`Monohel`), circles (`Bihel`), plus symbols (`Mixhel`), triangles (`Angfluc`), and stars (`Radfluc`).

The figure demonstrates that magnetic helicity generates an extremely small chiral charge Q_5, approximately 20 orders of magnitude smaller (not shown here; see Figure 5 of [1] for reference), which remains nearly constant over time. This small but finite Q_5 provides the chiral asymmetry that drives the CME and, consequently, influences the magnetic field evolution. Its small magnitude is set by strong spin-flip damping; without it, Q_5 would grow to values comparable to the magnetic helicity. The figure also confirms that the simulations satisfy the generalized helicity conservation law (Eq. 4). In particular, the evolution of the total helicity is well balanced by the spin-flip term, i.e., changes in $|Q_5+\frac{\alpha}{\pi\,\hbar\,c}\,\chi_M|$ are closely compensated by $|\Gamma_5\,\Delta t|$, as predicted by theory. Minor early-time discrepancies (during the first few years) arise from transient adjustments and small surface helicity fluxes ($\propto \mathbf{E}\times\mathbf{A}$) introduced by the boundary conditions. These effects decay rapidly as the system relaxes. Reducing the time step improves conservation but at a significant computational cost; nevertheless, helicity is conserved to a satisfactory level for this analysis.

Figure 4 also shows the time evolution of the dimensionless fractional helicity, $\tilde{\chi}$ (dots, right y-axis, purple), defined as

$$\tilde{\chi} = \frac{k_{\rm min}\,|\chi_M|}{2E_{\rm M}}, \tag{11}$$

where $k_{\rm min} \equiv 2\pi/R_{\rm crust}$ is the smallest wavenumber allowed by the domain, with $R_{\rm crust}$ representing the largest spatial scale of the system. This definition normalizes the magnetic helicity to the maximum value attainable at the system scale. By construction, $\tilde{\chi} \approx 1$ corresponds to a configuration approaching the maximum helicity allowed at the largest scale (i.e., a fully helical, nearly force-free field), whereas $\tilde{\chi} \ll 1$ indicates that the magnetic field carries little magnetic helicity at the system scale, either due to intrinsically low helicity, cancellation between opposite helicities, or helicity confined to small scales. An increase in $\tilde{\chi}$ therefore indicates a relative enhancement of magnetic helicity at the largest spatial scale. In all simulations presented here, including the `Monohel` run, $\tilde{\chi}$ remains well below unity. The initial helicity content nevertheless differs significantly between runs: `Monohel` has the largest value, followed by `Mixhel` (approximately 10% of `Monohel`), `Bihel` ($\sim 3.5\%$), `Angfluc` ($< 1\%$), and `Radfluc` ($\sim 0.2\%$), as summarized in Table I.

The evolution of $\tilde{\chi}$ exhibits distinct behaviors across the different runs. In `Monohel`, $\tilde{\chi}$ remains approximately constant, with only a slight decrease over time. A similar trend is observed in `Mixhel` and `Bihel`, where both runs show a modest early-time increase before saturating at comparable values (see also Table I). This suggests that the magnetic helicity is not significantly redistributed across spatial scales and remains relatively weak at the largest scales. In contrast, the `Angfluc` and `Radfluc` runs exhibit a pronounced increase in $\tilde{\chi}$, growing by roughly an order of magnitude over time, indicating a progressive transfer of magnetic helicity toward larger spatial scales. As a result, the large-scale magnetic field becomes increasingly helical compared to both the other simulations (`Monohel`, `Bihel`, and `Mixhel`) and the smaller-scale structures within each run. This has important implications: it may be speculated that large-scale helical fields can drive the generation of chiral asymmetry via generalized helicity conservation (Eq. 4), rather than relying on initially smaller-scale structures, thereby potentially leading to a faster dissipation of the large-scale fields formed through the CME compared to standard

Ohmic decay. To support this hypothesis, we further examine the magnetic helicity and energy spectra (Figure 5) and the evolution of the dipolar magnetic field (Figure 6) in what follows.

The magnetic helicity spectrum is defined as

$$\chi_M(\ell, m; t) = 2 \int \ell(\ell+1)\Phi_{\ell m}\Psi_{\ell m} dr, \tag{12}$$

while the magnetic energy spectrum is given by

$$E_{\rm M}(\ell, m; t) = \frac{1}{2} \int \frac{\ell(\ell+1)}{r^2} \left[\frac{\ell(\ell+1)}{r^2} \Phi_{\ell m}^2 + {\Phi'_{\ell m}}^2 + \Psi_{\ell m}^2 \right], \tag{13}$$

where, $\Phi'_{\ell m} = \partial \Phi_{\ell m}/\partial r$. These expressions lead to the spectral realizability condition,

$$k\, \chi_M(\ell) \leq 2\, E_{\rm M}(\ell), \tag{14}$$

with the pseudo-wavenumber defined as $k = \sqrt{\ell(\ell+1)}/R$, where R is the radius of the computational domain. This condition must be satisfied at all times for each spherical harmonic degree ℓ.

The left panels of Figure 5 show the evolution of $k\,\chi_M(\ell, t)/2$ over the first 1000 yr of neutron star evolution as a function of spherical harmonic degree ℓ (horizontal axis) and time (vertical axis), with color indicating the amplitude. The right panels display the corresponding magnetic energy spectra, $E_{\rm M}(\ell)$, as a function of ℓ at different times, with color representing the temporal evolution. Throughout the evolution, we verify that the realizability condition is satisfied, i.e. $k\,\chi_M(\ell, t)/2 \leq E_{\rm M}(\ell, t)$ for all times and harmonic degrees ℓ, ensuring the physical consistency of the results.

At $t = 0$, $k\,\chi_M(\ell, t = 0)/2$ is predominantly concentrated at small spatial scales, mainly in the range $10 \lesssim \ell \lesssim 55$, depending on the specific simulation. In the helicity-free runs (`Bihel`, `Mixhel`, `Angfluc`, and `Radfluc`), both positive and negative contributions are present, leading to an overall cancellation of the net magnetic helicity, whereas in the `Monohel` run the multipolar components predominantly carry negative helicity. The initial magnetic helicity is approximately conserved throughout the evolution, although a few individual spherical-harmonic multipoles undergo sign changes over time. At the initial time, the large-scale structures are nearly non-helical in all simulations. Similarly, the smallest resolved scales ($60 \lesssim \ell \lesssim 70$) also carry negligible helicity. The magnetic energy (right panels) is likewise concentrated at small scales, with the initial spectrum approximately following $E_{\rm M}(\ell) \propto \ell^4$, and only weak contributions from large-scale modes.

As the system evolves, magnetic helicity is progressively redistributed from the initially helical small-scale structures toward both larger and smaller spatial scales that initially carry little or no helicity. This evolution is accompanied by a concurrent redistribution of magnetic energy across multipoles, following a similar pattern. The rate of this redistribution differs between the simulations. In the helicity-free runs, the transfer of both helicity and energy toward large-scale structures (e.g., dipole, $\ell = 1$) proceeds rapidly, typically within about a decade (see left panels), with a noticeable redistribution of magnetic energy already occurring within the first year (see right panels). In contrast, in the helical run (`Monohel`) the same redistribution is significantly delayed: a substantial transfer of helicity to the dipolar component appears only after nearly a century, while during the first year the evolution of the magnetic energy-spectrum slope remains markedly weaker than in the helicity-free cases.

The slope of the magnetic energy spectrum gradually converges toward a common spectral scaling, $E_{\rm M}(\ell) \propto \ell$, for all simulations, suggesting that an inverse-like cascade has taken place and indicating that each spherical-harmonic mode saturates independently at a characteristic energy level. Despite this redistribution, in an inverse-like cascade, small-scale structures remain dominant in the magnetic field configuration throughout the evolution. This behavior differs from the standard MHD inverse cascade, which is typically characterized by a shift of the spectral peak toward lower ℓ while approximately preserving the initial spectral slope [21, 31][5].

An amplification of the large-scale magnetic structures ($\ell \lesssim 10$) occurs in all simulations, but it differs between runs. In the `Monohel` and `Bihel` runs, the large-scale structures, once established, remain stable over time, with energy dissipation occurring predominantly in the smaller-scale structures. By contrast, in the `Mixhel` run, the large-scale structures undergo slight dissipation at later times compared to `Monohel` and `Bihel`. A more pronounced dissipation of the formed large-scale structures is clearly seen in the `Angfluc` run and becomes even stronger in `Radfluc`. In these latter two cases, the dissipation of the large-scale structures is clearly not driven by Ohmic diffusion alone, but also by the CME. This is evident from the fact that all scales decay at a comparable rate, whereas in the case of pure Ohmic diffusion, large-scale magnetic structures would evolve more slowly ($\tau_d \approx L^2/\eta$, where L is a characteristic magnetic length scale, implying slower dissipation for larger structures). This behavior also extends to the smallest scales generated by the CME ($\ell \gtrsim 55$), which follow a similar dissipation pattern.

We relate this behavior to the redistribution of magnetic helicity toward larger spatial scales, which is not uniform across all runs, as already indicated by the time evolution of $\tilde{\chi}$ in Figure 4. Focusing on the dipolar component—both to avoid conflating contributions from multiple scales and due to its particular relevance for magnetar applications—we find that in the `Monohel` and `Bihel` simulations it initially develops a modest level of helicity, which then decreases at later times. This is consistent with an ongoing exchange of magnetic helicity be-

[5] The extent of the inverse cascade under the non-linear Hall term in neutron stars is limited by the inverse aspect ratio of the neutron star crust, $\mathcal{A} \approx 1/30$, making it ineffective in forming large-scale structures ($\ell = 1$), despite its presence [21].

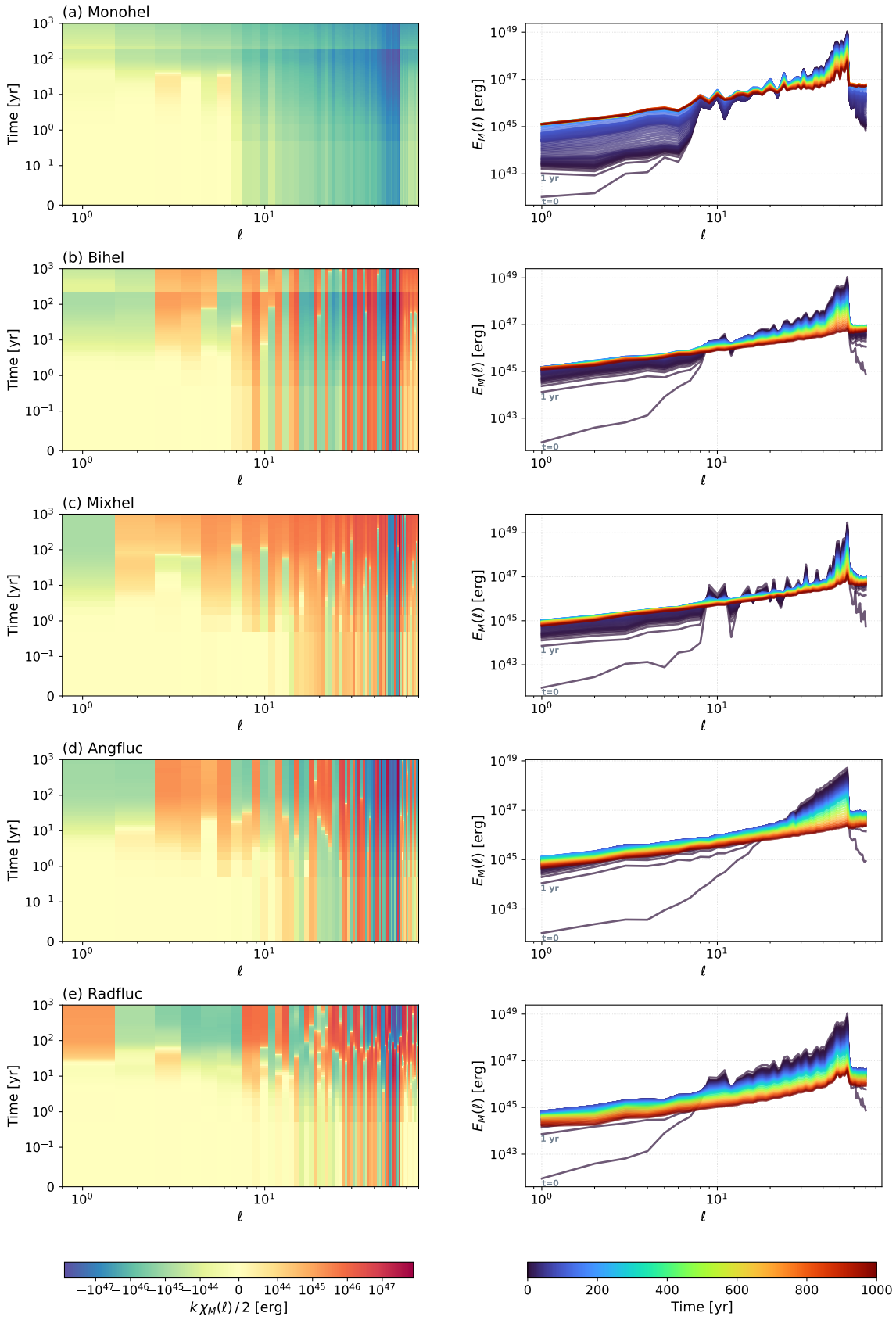

FIG. 5: Magnetic helicity and energy spectra for the five simulations: (a) `Monohel`, (b) `Bihel`, (c) `Mixhel`, (d) `Angfluc`, and (e) `Radfluc`. The left column shows the magnetic helicity spectrum $k\,\chi_M(\ell,t)/2$ as a function of spherical harmonic degree ℓ and time, with color indicating the helicity amplitude. The right column shows the magnetic energy spectrum $E_M(\ell)$ versus ℓ at different times, with color encoding time.

tween the dipole and smaller-scale multipoles, allowing the dipolar field to be continuously replenished and thus sustained.

By contrast, in the `Angfluc` and `Radfluc` runs—where the dipole ultimately decays after the magnetic energy stored in the $\ell = 1$ mode reaches $\sim 10^{45}$ erg, corresponding to the maximum energy attainable by the dipolar component through the CME (noting the convergence of this value across all runs, as shown in the right panels of Figure 5)—the helicity contained in the dipolar component becomes comparatively large at later times ($t \gtrsim 100$ yr), particularly in the `Radfluc` case. In this regime, the dipole acts as an intermediate reservoir that transfers helicity to smaller scales through the CME, thereby contributing to the destabilization of the large-scale field. These results are consistent with the evolution of $\tilde{\chi}$ (Figure 4), where the pronounced late-time increase—particularly in the `Radfluc` and `Angfluc` runs—indicates a progressive accumulation of helicity within the large-scale magnetic field structure, in contrast to the behavior observed in the `Monohel` and `Bihel` cases.

B. Magnetic field analysis

The time evolution of the volume-averaged magnetic field and its dipolar component is shown in Figure 6. The color bar in the left panel indicates $|\mu_5^{\rm avg}|$, while the right panel shows the evolution of $\mu_5^{\rm max}$. Different simulation runs are denoted by solid lines with distinct markers. The `NoCME` run is shown in black, as the CME is switched off.

The volume-averaged magnetic field (left panel of Figure 6) is initially $B_{\rm rms} \simeq 3\times10^{16}$ G in all simulations and decays over time. When accounting for the CME, which is sourced by the topology of the magnetic field, the effect is a redistribution of magnetic energy across spatial scales rather than amplification of the mean field (see Figure 5), with the decay rate depending on the specific simulation. In the `NoCME` run, where only Ohmic dissipation operates, the magnetic field decays exponentially as $\propto \exp(-t/\tau_{\rm d})$, with $\tau_{\rm d} \equiv 1/(k^2\eta) \approx 20$–$25$ yr. Here, k denotes the Fourier wavenumber of a representative mode, with $k \sim 1/L$. All modes decay in this case, including the initially weak dipolar component, which decays from 4.0×10^{12} G to 1.3×10^{11} G over 100 years.

In the remaining simulations, when the CME is accounted for, the decay departs from purely Ohmic behavior and follows $\propto \exp(-t/\tau_{\rm eff})$, with an effective dissipation timescale

$$\tau_{\rm eff} \approx \frac{\tau_d}{1-\dfrac{|k_5|}{k}}. \tag{15}$$

This expression reflects the competition between Ohmic dissipation and the CME. For $k \gg |k_5|$ (very small scales), $\tau_{\rm eff} \approx \tau_{\rm d}$ and the CME is negligible. For $k \gtrsim |k_5|$ (intermediate scales), dissipation is suppressed and $\tau_{\rm eff} > \tau_{\rm d}$. In the limiting case $k \to |k_5|$ (characteristic scale), $\tau_{\rm eff} \to \infty$, corresponding to complete suppression of dissipation. The regime $k < |k_5|$ (large scales), which would lead to growth, is not realized in our setup, as $k_5 \approx k/(1 + B^2_{\rm QED}/B^2)$ implies that $k_5 < k$ at all times.

The color variation of the curves in the left panel of Figure 6 represents different values of $|\mu_5^{\rm avg}|$. We plot the absolute value since its sign depends on the relative orientation of the electric and magnetic fields; the corresponding sign for each run is reported in Table I. The magnitude of $|\mu_5^{\rm avg}|$ is primarily determined by the initial magnetic-field configuration and remains approximately constant throughout the evolution, with a slight decay at later times ($t \gtrsim 200$ years). The largest values are obtained in the `Monohel` run, reaching $\sim 10^{-12}$ MeV, while the other configurations (`Mixhel`, `Bihel`, `Angfluc`, and `radfluc`) lie in the range $\sim 10^{-13}$–10^{-15} MeV. In the `NoCME` case, $\mu_5^{\rm avg} = 0$ by construction. A clear trend is observed whereby larger values of $|\mu_5^{\rm avg}|$ are associated with slower magnetic-field decay, with the exception of the `Mixhel` case. This suggests that the decay rate in the effective dissipation timescale $\tau_{\rm eff}$ (see Eq. (15)), which is controlled by the chiral parameter $|k_5|$, correlates with $|\mu_5^{\rm avg}|$, with $|k_5| \equiv |k_5|^{\rm avg}$.

The time evolution of the dipolar field, shown in the right panel of Figure 6, differs among the various runs. In the `NoCME` case, no amplification of the dipolar component is observed, as the CME is inactive and therefore no redistribution of magnetic energy across spatial scales occurs. This behavior is consistent with $\mu_5 = 0$, indicated by the black curve. In contrast, all other simulations show a clear growth of the dipolar field, correlated with the chiral asymmetry (see also colorbar).

The growth of the dipolar field proceeds in distinct stages and differs between runs. During the early phase ($t \lesssim 0.1$ yr), all simulations show only a marginal increase, as the chiral asymmetry is still developing from the initially turbulent magnetic field configuration. This growth is slightly more pronounced in the helicity-free runs (`Bihel`, `Mixhel`, `Angfluc`, and `Radfluc`). In the `Monohel` case, which has net initial magnetic helicity, this initial stage is followed by a gradual growth phase over several decades and subsequently by an exponential amplification phase extending over longer timescales. We interpret this latter stage as the onset of the CMI, with growth approximately following $\propto \exp(t/\tau_5)$, where $\tau_5 \equiv 1/(\eta k|k_5|)$. In contrast, the helicity-free runs enter the exponential growth phase earlier (within ~ 1 yr after neutron star formation) and evolve more rapidly. This highlights a clear qualitative difference between systems with and without net initial magnetic helicity.

Following the onset of the CMI, the dipolar field saturates at $B \gtrsim 10^{14}$ G. In all cases, the dipolar component does not exceed a few $\times10^{14}$ G, indicating a robust saturation level that is largely insensitive to the initial conditions. This behavior is also reflected in the slope of the magnetic energy spectra shown in the right column of Figure 5. In particular, both the `Monohel` and `Bihel`

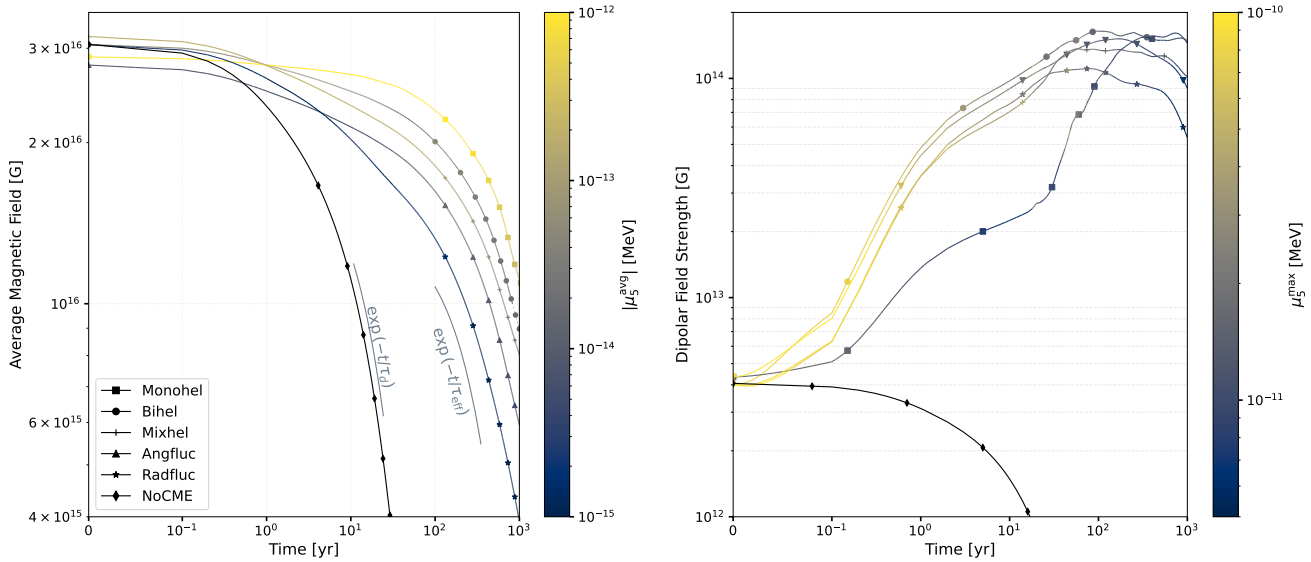

FIG. 6: Magnetic field evolution over the first 10^3 years. The left panel shows the volume-averaged magnetic field, while the right panel shows the mean dipolar magnetic field. The simulation runs are represented by solid lines with distinct markers (as in Figure 4). In the left panel, the colorbar corresponds to the average chiral chemical potential, $\mu_5^{\rm avg}$, while in the right panel it corresponds to the maximum chiral chemical potential, $\mu_5^{\rm max}$. The `NoCME` run is shown in black (with diamond markers), as it does not include the CME.

runs reach saturation at $B \simeq 1.5 \times 10^{14}$ G, although on different timescales: after ~ 200 yr in the `Monohel` case and ~ 50 yr in the `Bihel` case. After saturation, the resulting dipolar field is stable and subsequently decays through standard Ohmic dissipation. These results indicate that the CME can generate magnetar-strength dipolar fields independently of whether the initial magnetic field is helical or helicity-free.

A distinct late-time behavior (i.e., once the 10^{14} G dipole has already formed) is observed in the helicity-free runs. In the `Mixhel` case, the resulting dipole is slightly weaker than in `Bihel`; it stabilizes at 10^{14} G after approximately 1000 years, following a late-time decay phase between roughly 600 and 800 years, and subsequently evolves in a manner consistent with standard Ohmic decay. In contrast, in the `Angfluc` and `Radfluc` cases, the dipolar field enters a decay phase that is faster than expected from standard Ohmic dissipation alone; this accelerated decay sets in only once the dipolar field reaches a strength of $\approx 10^{14}$ G and develops magnetic helicity, as shown in the left panels of Figure 5. In this regime, magnetic energy is transferred from the large-scale dipolar component to smaller-scale structures, leading to a weakening of the dipole. In these two cases, the CME-generated dipole is therefore not stable. Its stability appears to depend on the initial spatial distribution of helicity in the system, where small-scale helicity fluctuations (as in `Angfluc` and `Radfluc`) seed the formation of transient helical dipoles, which are then more susceptible to fragmentation into smaller-scale magnetic structures.

To understand the different onset of the CMI in helicity-free and helical cases, we monitor $\mu_5^{\rm max}$ (see colorbar in the right panel of Figure 6). In helicity-free runs, $\mu_5^{\rm max}$ reaches values of order 10^{-10} MeV at early times and subsequently decreases to $\sim 10^{-11}$ MeV over several decades. In contrast, in the `Monohel` run, $\mu_5^{\rm max}$ starts at $\approx 10^{-11}$ MeV and remains approximately constant over the entire simulated time span. This suggests that the onset of the CMI may be governed by the magnitude of $\mu_5^{\rm max}$, although this remains speculative.

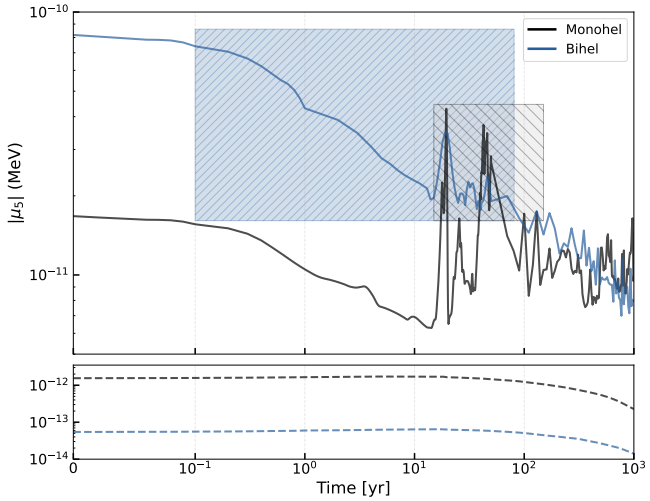

FIG. 7: Time evolution of the absolute value of the mean (lower panel, dashed lines) and maximum (upper panel, solid lines) of μ_5 for the `Monohel` (black) and `Bihel` (blue) runs. The shaded regions indicate the time intervals during which the CMI is active in each case.

To further test this hypothesis, Figure 7 shows the time evolution of μ_5 for the `Monohel` and `Bihel` runs, including both the volume-averaged value (lower panel, dashed lines) and the maximum value (upper panel, solid lines). The shaded regions mark the time intervals during which the CMI actively contributes to the growth of a $\sim 10^{14}$ G dipolar field. Once the dipole is established, the shading is terminated, although the CMI may still operate to sustain the field.

The volume-averaged value, $\langle\mu_5\rangle$, decays slowly and plays a minor role in triggering the instability. In contrast, $\mu_5^{\rm max}$ exhibits a different behavior: in the `Bihel` run, it is initially large, leading to an early activation of the CMI within $\lesssim 1$ yr after neutron star formation, after which it gradually decreases and the CME becomes less efficient. In the `Monohel` case, $\mu_5^{\rm max}$ is initially smaller by a factor of ~ 5, and no significant amplification occurs at early times; however, a later enhancement in $\mu_5^{\rm max}$ occurs, coinciding with the onset of CMI. Notably, in `Monohel`, $\mu_5^{\rm max}$ does not exhibit a sustained decay, but rather a transient increase associated with the instability.

These results indicate that *(i)* the onset of the CMI is governed by $\mu_5^{\rm max}$ rather than its volume average, and *(ii)* a threshold value $\mu_5^{\rm max} \gtrsim 2\times10^{-11}$ MeV is required to trigger the instability, although this estimate remains approximate. Accordingly, the characteristic timescale can be expressed in terms of $k_5^{\rm max}$ as

$$\tau_5 \equiv \frac{1}{\eta\, k\, |k_5^{\rm max}|} \equiv \frac{L}{\eta\, |k_5^{\rm max}|} \tag{16}$$

reflecting that the evolution is governed by the maximum value of the chiral chemical potential.

C. Timescales

In the present simulations, the Hall term is neglected for two main reasons. First, our goal is to isolate the effects of the CME for different magnetic field configurations and helicity contents. This becomes challenging when both effects are included, since both mechanisms can transfer magnetic energy across spatial scales; their simultaneous inclusion would therefore hinder a clear separation of their individual contributions. Second, including both effects poses a numerical challenge, as such simulations require more advanced techniques than those currently implemented in the `MATINS` code. To our knowledge, the combined action of the Hall term and the CME has not yet been explored in the literature.

To determine at which stage of the evolution the Hall term may become important, we examine the characteristic timescales in the neutron star crust. These include the Ohmic diffusion timescale (τ_d, dashed black line), the chiral timescale (τ_5, solid black line), and the Hall drift timescale ($\tau_h \equiv L^2/f_h B_{\rm rms}$, dotted black line), as shown in Figure 8 over the first 200 years of evolution. The color bar indicates the cooling of the mean temperature, while the vertical green dashed lines mark the epochs at

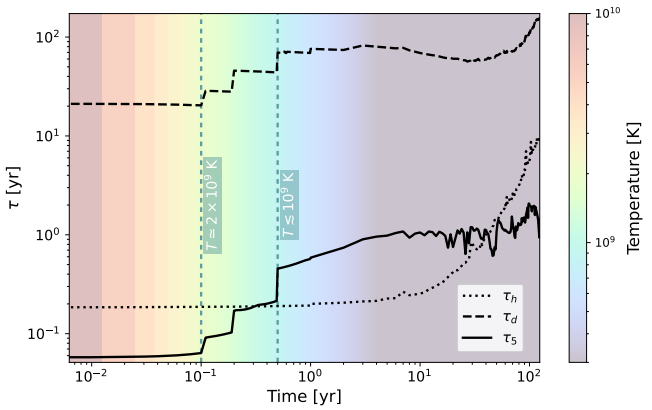

FIG. 8: Time evolution of the characteristic timescales in the neutron star crust for the `Radfluc` run. The dotted, dashed, and solid black curves correspond to the Hall (τ_h), Ohmic (τ_d), and chiral (τ_5) timescales, respectively. The color bar denotes the mean temperature evolution. Vertical green dashed lines indicate the epochs at which the temperature reaches $T \simeq 3\times10^9$ K and $T \simeq 10^9$ K.

which the temperature reaches approximately 2×10^9 K and 10^9 K, respectively. The results are shown for the `Radfluc` run.

During the early phase, the neutron star undergoes thermal relaxation, during which the temperature decreases rapidly from $\sim 10^{10}$ K to $\sim 10^9$ K as the crust and core approach a quasi-isothermal equilibrium [49, 54]. This rapid cooling is reflected in the evolution of the magnetic diffusivity, which decreases as the star cools and directly impacts the Ohmic and chiral timescales, τ_d and τ_5, through their dependence on η. The jumps observed in τ_d and τ_5 reflect variations in the magnetic diffusivity, which are most pronounced at early times and gradually diminish as the star evolves. These variations are computed self-consistently within the `MATINS` code. In contrast, the Hall timescale remains largely unaffected by the temperature evolution.

The Ohmic timescale is several orders of magnitude longer (i.e., slower) than both the Hall and chiral timescales. In contrast, the Hall and chiral timescales exhibit a strong interplay. During the first few months of the neutron star's evolution, the chiral process operates on a shorter timescale than the Hall drift. As the star cools during thermal relaxation, there is a brief period ($t \approx 0.2$–0.5 yr) in which the two timescales become comparable. Subsequently, as cooling proceeds, the chiral timescale becomes longer than the Hall timescale, which becomes shorter by roughly a factor of two. This regime persists for a few decades, until the star reaches an age of approximately several tens of years, at which point the Hall timescale increases significantly (i.e., the Hall evolution slows down), whereas the chiral timescale remains nearly constant, with only a gradual increase due to the slow decrease of $k_5^{\rm max}$.

The divergence between the timescales at this stage results from the CME transferring magnetic energy to larger scales, which leads to a rapid increase in the characteristic magnetic length scale L. Since $\tau_h \propto L^2$ and $\tau_5 \propto L$, the growth of L affects the Hall timescale more strongly, leading to its pronounced increase. The same effect also applies to the Ohmic timescale ($\tau_d \propto L^2$), which becomes progressively longer as L increases.

Finally, we note that in the present evolution we do not explicitly account for changes in the characteristic magnetic length scale L induced by the Hall effect. This may affect the evolution of the timescales depending on the initial conditions, in particular on whether the initial magnetic field supports an inverse cascade driven by the Hall term [21, 31] or instead favors a direct cascade [39, 47]. We further emphasize that the Hall timescale does not depend directly on the magnetic helicity content or its distribution; this information is instead encoded in $k_5^{\max}$ and, consequently, in the chiral timescale. This distinction is important because, in regions where the CME is most effective, the magnetic field is aligned with the electric current (see Section II A). As a result, in locally force-free regions, the Hall term is not expected to significantly affect the CME-driven evolution. A fully self-consistent treatment of the coupled Hall and CME dynamics will be addressed in a follow-up study.

V. DISCUSSION

In the presence of a very strong magnetic field, $B \gtrsim B_{\rm QED}$, electrons occupy the LLL, and their motion becomes effectively one-dimensional along the magnetic field lines. As the magnetic field untwists, an electric field is induced, leading to $\boldsymbol{E} \cdot \boldsymbol{B} > 0$. This drives the chiral anomaly: electrons undergo momentum reversal, effectively transferring right-handed states into left-handed ones, while left-handed electrons are promoted to higher Landau levels. Once outside the LLL, chirality-flipping processes further reduce the chiral asymmetry (see Figure 1). Nevertheless, even a small chiral asymmetry, $\mu_5 \sim 10^{-11}\,\mathrm{MeV}$, can significantly modify the magnetic field evolution by redistributing magnetic energy across spatial scales.

This mechanism has been shown to be effective in the long-term evolution of neutron stars hosting helical magnetic fields [1]. However, the magnetic helicity content at birth remains uncertain. Standard MHD processes operating during the dynamo phase of neutron star formation preserve reflection symmetry, thereby permitting magnetic energy amplification without modifying the net magnetic helicity [25]. By contrast, net helicity may be generated during core collapse if the CME operates during the proto-neutron star phase [17]. This process, however, is likely suppressed by spin-flip reactions, which rapidly damp the chiral imbalance on the short dynamical timescales characteristic of proto-neutron stars [8, 11]. In this regime, any residual chiral asymmetry, comparable to that expected during later neutron star evolution, is insufficient to sustain significant helicity growth. Motivated by these uncertainties, we consider a range of small-scale magnetic configurations representative of newborn neutron stars, as predicted by dynamo models [15], and investigate CME-driven evolution for different initial helicity distributions, including non-helical configurations.

We find that the CME efficiently generates magnetar-strength dipolar fields on decadal timescales by transferring magnetic energy from small-scale structures to large scales. This behavior is largely independent of whether the initial field is helical or not. In all cases considered here, the magnetic energy spectrum evolves toward a common scaling, $\mathcal{E}_M(\ell) \propto \ell$, indicating scale-by-scale saturation of spherical harmonic modes, with the dipole component reaching energies of a few 10^{45} erg. A key result is that dipole amplification from $\sim 10^{12}$ G to magnetar levels of $\sim 10^{14}$ G occurs robustly in all initial configurations considered.

We further find that non-helical field configurations are more efficient at triggering rapid dipole growth than initially helical ones. The onset of the CMI is primarily driven by localized helical structures that generate a residual chiral asymmetry and is mainly controlled by the maximum chiral chemical potential, $\mu_5^{\max}$, while the volume-averaged value plays a subdominant role, consistent with results in cosmological contexts [55, 56]. In particular, the instability requires ($\mu_5^{\max} \gtrsim \mathrm{few}\times 10^{-11}\,\mathrm{MeV}$) to operate efficiently in the magnetar regime, thereby enabling the formation of strong dipolar fields of order 10^{14} G.

Once a $\sim 10^{14}$ G dipole is formed, its subsequent evolution depends sensitively on the initial helicity distribution, namely the local sign and coherence of $\boldsymbol{A} \cdot \boldsymbol{B}$. In some cases, these dipoles remain stable and evolve primarily through standard Ohmic decay, while in others they become unstable after acquiring sufficient helicity, leading to CME-driven dissipation and transfer of magnetic energy toward less helical modes. We find that this behavior correlates with the initial helicity structure: configurations with large coherent helicity patches (e.g., `Monohel`, `Bihel`, and `Mixhel`) produce stable dipoles, whereas highly fragmented helicity distributions (e.g., `Radfluc` and `Angfluc`) tend to generate unstable helical dipoles. In the latter cases, the chiral chemical potential fluctuates rapidly between positive and negative values on short spatial scales, preventing the formation of coherent regions with sufficiently large $\mu_5^{\max}$ to sustain the instability. These sign reversals effectively average out the chiral asymmetry, thereby suppressing the CME. This behavior is particularly evident in the `Radfluc` model, where helicity reversals occur on scales of ~ 0.06 km within a crustal thickness of ~ 0.86 km.

Overall, our results provide a robust pathway for magnetar formation in which initially small-scale, magnetar-strength magnetic fields—provided that the CME growth timescale is shorter than the Ohmic dissipation timescale (see Figure 8)—can be reorganized into large-scale dipo-

lar fields through the CME, independent of whether the magnetic field has net helicity. The CME should therefore be systematically included in studies of magnetic field evolution in neutron-star interiors, particularly in magnetars, as its impact is self-regulated by the local properties of the system.

To address why not all neutron stars become magnetars and to account for the diversity of isolated neutron-star classes, we note that if dynamo action amplifies the magnetic field to magnetar strength on small spatial scales, the outcome is primarily determined by the helicity distribution. This determines whether the resulting large-scale field (i.e., the dipole) remains stable, leading to magnetar-like behavior, or becomes unstable and decays over time, potentially giving rise to other classes such as low-field magnetars or Central Compact Objects, characterized by relatively weak dipolar fields despite strong internal magnetic energy. By contrast, if the initial magnetic field is relatively weak at birth, as expected for typical rotation-powered pulsars, the CME is not triggered, preventing any significant redistribution of magnetic energy. These results highlight the importance of the magnetic helicity distribution at birth in proto-neutron star dynamo models, which have so far focused primarily on magnetic field configurations while largely neglecting helicity. Both the field structure and helicity distribution established at birth are therefore crucial initial conditions that determine the subsequent evolutionary pathway and observational class of neutron stars. Finally, future studies should incorporate additional physical processes, in particular the combined evolution of the CME and the Hall effect, in models of neutron-star magnetic field evolution.

DATA AVAILABILITY

The `MATINS` code is freely available at https://github.com/ice-csic-astroexotic/MATINS.
An extended version of the code, including the effects of the chiral anomalies considered here, can be provided upon reasonable request. The reduced simulation output data are available on Zenodo at https://doi.org/10.5281/zenodo.19920753.

ACKNOWLEDGMENTS

CD thanks Matthias Reinhardt, Naoki Yamamoto, Axel Brandenburg, Jennifer Schober, Jose Pons, and Stefano Ascenzi for helpful discussions. CD is supported by the Ministerio de Ciencia, Innovación y Universidades (JDC2023-052227-I), co-funded by AEI (MCIN/AEI/10.13039/501100011033), the FSE+, and the Universidad de Alicante. CD also acknowledges support from the Conselleria d'Educació, Cultura, Universitats i Ocupació de la Generalitat Valenciana (grant CIPROM/2022/13) and the AEI grant PID2021-127495NB-I00.

Appendix A: Initial magnetic field and helicity distribution

To define the initial magnetic field configurations described in Section III, we decompose the magnetic field into poloidal ($\boldsymbol{B}_p$) and toroidal ($\boldsymbol{B}_t$) components [57]:

$$\boldsymbol{B} = \boldsymbol{B}_p + \boldsymbol{B}_t, \tag{A1}$$

$$\begin{aligned} \boldsymbol{B}_t &= -\boldsymbol{r}\times\boldsymbol{\nabla}\Psi, \qquad \boldsymbol{A}_t = -\boldsymbol{r}\times\boldsymbol{\nabla}\Phi, \\ \boldsymbol{B}_p &= \boldsymbol{\nabla}\times\boldsymbol{A}_t = -\boldsymbol{r}\Delta\Phi + \boldsymbol{\nabla}\frac{\partial}{\partial r}\left(r\Phi\right), \end{aligned} \tag{A2}$$

where $\boldsymbol{A}_t$ is the toroidal vector potential. The two scalar functions $\Phi(\boldsymbol{r},t)$ and $\Psi(\boldsymbol{r},t)$ uniquely define the poloidal and toroidal components, respectively. Next, we expand the scalar functions in spherical harmonics [58]:

$$\begin{aligned} \Phi(t,r,\theta,\phi) &= \frac{1}{r}\sum_{\ell m}\Phi_{\ell m}(r,t)Y_{\ell m}(\theta,\phi), \\ \Psi(t,r,\theta,\phi) &= \frac{1}{r}\sum_{\ell m}\Psi_{\ell m}(r,t)Y_{\ell m}(\theta,\phi), \end{aligned} \tag{A3}$$

where $\ell = 1,2,\ldots$ denotes the multipole degree and $m = -\ell,\ldots,\ell$ the azimuthal order.

We define the radial dependence of the poloidal scalar function at $t=0$ as

$$\Phi_{\ell m}(r) = \Phi^0_{\ell m}\, k_r\, r\,(a + \tan(k_r R)\, b), \tag{A4}$$

where the coefficients a and b are determined by imposing the inner and outer boundary conditions. The radial wavenumber k_r is taken in the range $k_r \approx 400$–$450\,\mathrm{km}^{-1}$, chosen to balance the fastest-growing CME modes against Ohmic dissipation (see also Figure 3 of Dehman and Pons [1]). This choice is particularly important in the radial direction, where both processes are highly sensitive to microphysical properties that vary strongly with density.

The coefficient $\Phi^0_{\ell m}$ is a normalization factor evaluated at a reference radius just beneath the stellar surface. For each (ℓ, m), it specifies the amplitude and phase of the corresponding poloidal mode, thereby controlling the distribution of magnetic energy across spatial scales. An analogous role is played by the toroidal normalization factor $\Psi^0_{\ell m}$. Together, $\Phi^0_{\ell m}$ and $\Psi^0_{\ell m}$—through their relative amplitudes and phases—govern the local sign and spatial structure of the magnetic helicity. Varying these coefficients therefore provides a direct way to construct different initial helicity distributions.

For the `Monohel` configuration, in which an initial net magnetic helicity is imposed, the poloidal and toroidal components are intrinsically linked by construction [21].

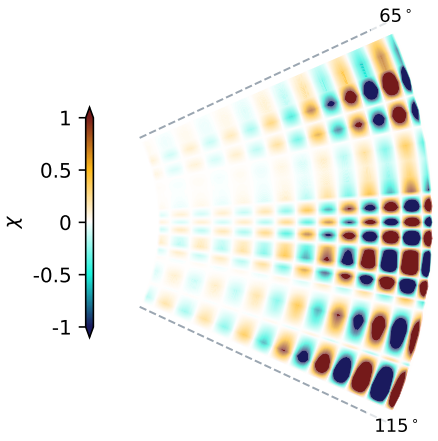

FIG. 9: Meridional profile of the initial local magnetic helicity χ, normalized by its maximum absolute value, for the `Radfluc` run in the angular interval $65° \leq \theta \leq 115°$. The crustal region is shown with a radial magnification factor of 8 for clarity.

Accordingly, we define the radial toroidal scalar function $\Psi(r, t{=}0)$ as

$$\Psi_{\ell m}(r) = \alpha_{\ell m}\, \Phi_{\ell m}(r), \tag{A5}$$

where, for a conservative choice, we adopt $\alpha_{\ell m} = k_{\rm ang} = \sqrt{\ell(\ell+1)}/R$, with R denoting the radius at the surface of the computational domain. For a maximally helical configuration, one instead sets $\alpha_{\ell m} = k$, where $k = k_r + k_{\rm ang}$. Note that, in the `Monohel` configuration, the normalization factors satisfy $\Psi^0_{\ell m} = \Phi^0_{\ell m}$.

To avoid imposing an initial net magnetic helicity by construction, we define the normalized poloidal and toroidal coefficients, $\Phi^0_{\ell m}$ and $\Psi^0_{\ell m}$, independently—that is, without introducing correlations between them—for the `Bihel`, `Mixhel`, and `Angfluc` runs. We also ensure that the characteristic angular scale of magnetic helicity structures decreases across these runs by progressively favoring higher spherical-harmonic modes (see the left panels of Figure 5). In the `Bihel` run, opposite signs of magnetic helicity are enforced between the northern and southern hemispheres, producing mirror-symmetric configurations that cancel globally and therefore yield a negligible net helicity. In the `Mixhel` and `Angfluc` simulations, random signs are assigned to the local helicity of each (ℓ, m) mode, resulting in configurations with vanishing net helicity (see Figures 3 and 5).

For the `Radfluc` run, we adopt the same $\Phi^0_{\ell m}$ and $\Psi^0_{\ell m}$ as in the `Bihel` run, but assign different radial wavenumbers to the poloidal and toroidal scalar functions, with $k_r^{\rm pol} \approx 400$ and $k_r^{\rm tor} \approx 450$. This introduces small-scale, localized helicity fluctuations in the radial direction while maintaining an approximately vanishing net helicity. Figure 9 shows the meridional profile of the normalized local magnetic helicity, $\chi(r, \theta, \phi, t_0)$, in the angular interval $65° \leq \theta \leq 115°$, highlighting strong spatial variations of magnetic helicity across the crust.

Finally, we employ curl operators within a finite-volume scheme adapted to cubed-sphere coordinates [47] and compute the magnetic field components from the poloidal and toroidal scalar functions using Eq. (A2). This procedure guarantees an initial magnetic field that is divergence-free (to machine precision) and free of coordinate singularities.

[1] C. Dehman and J. A. Pons, Phys. Rev. Res. **7**, 033231 (2025).
[2] A. Ohnishi and N. Yamamoto, arXiv e-prints , arXiv:1402.4760 (2014), arXiv:1402.4760 [astro-ph.HE].
[3] N. R. Poniatowski, American Journal of Physics **87**, 436–443 (2019).
[4] S. L. Adler, Physical Review **177**, 2426 (1969).
[5] J. S. Bell and R. Jackiw, Nuovo Cimento A Serie **60**, 47 (1969).
[6] D. S. Freed, arXiv e-prints , arXiv:2107.03557 (2021), arXiv:2107.03557 [math.HO].
[7] A. Boyarsky, J. Fröhlich, and O. Ruchayskiy, Phys. Rev. Lett. **108**, 031301 (2012), arXiv:1109.3350 [astro-ph.CO].
[8] D. Grabowska, D. B. Kaplan, and S. Reddy, prd **91**, 085035 (2015), arXiv:1409.3602 [hep-ph].
[9] G. Sigl and N. Leite, jcap **2016**, 025 (2016), arXiv:1507.04983 [astro-ph.HE].
[10] D. B. Kaplan, S. Reddy, and S. Sen, prd **96**, 016008 (2017), arXiv:1612.00032 [hep-ph].
[11] V. A. Skoutnev and A. M. Beloborodov, arXiv e-prints , arXiv:2603.07715 (2026), arXiv:2603.07715 [astro-ph.HE].
[12] S. A. Balbus and J. F. Hawley, Astrophys. J. **376**, 214 (1991).
[13] M. Obergaulinger, H. T. Janka, and M. A. Aloy, MNRAS **445**, 3169 (2014), arXiv:1405.7466 [astro-ph.SR].
[14] M. Á. Aloy and M. Obergaulinger, MNRAS **500**, 4365 (2021), arXiv:2008.03779 [astro-ph.HE].
[15] A. Reboul-Salze, J. Guilet, R. Raynaud, and M. Bugli, A&A **645**, A109 (2021), arXiv:2005.03567 [astro-ph.HE].
[16] Y. Masada, T. Takiwaki, and K. Kotake, Astrophys. J. **924**, 75 (2022), arXiv:2001.08452 [astro-ph.HE].
[17] J. Matsumoto, N. Yamamoto, and D.-L. Yang, prd **105**, 123029 (2022), arXiv:2202.09205 [astro-ph.HE].
[18] P. Barrère, J. Guilet, R. Raynaud, and A. Reboul-Salze, A&A **695**, A183 (2025), arXiv:2407.01775 [astro-ph.HE].
[19] C. Dehman, D. Viganò, S. Ascenzi, J. A. Pons, and N. Rea, MNRAS **523**, 5198 (2023), arXiv:2305.06342 [astro-ph.HE].
[20] A. Igoshev, P. Barrère, R. Raynaud, J. Guilet, T. Wood, and R. Hollerbach, Nature Astronomy **9**, 541 (2025), arXiv:2501.04768 [astro-ph.HE].
[21] C. Dehman and A. Brandenburg, A&A **694**, A39 (2025), arXiv:2408.08819 [astro-ph.HE].

[22] L. Woltjer, Proceedings of the National Academy of Sciences **44**, 489 (1958), https://www.pnas.org/doi/pdf/10.1073/pnas.44.6.489.
[23] J. B. Taylor, Phys. Rev. Lett. **33**, 1139 (1974).
[24] G. Bodo, F. Cattaneo, A. Mignone, and P. Rossi, The Astrophysical Journal **843**, 86 (2017).
[25] A. Brandenburg and K. Subramanian, Physics Reports **417**, 1 (2005).
[26] H. K. Moffatt, Journal of Fluid Mechanics **35**, 117 (1969).
[27] M. A. Berger and G. B. Field, Journal of Fluid Mechanics **147**, 133 (1984).
[28] V. I. Arnol'd and B. A. Khesin, Annual Review of Fluid Mechanics **24**, 145 (1992).
[29] A. A. Pevtsov, M. A. Berger, A. Nindos, A. A. Norton, and L. van Driel-Gesztelyi, Space Sci. Rev., **186**, 285 (2014).
[30] E. Pariat, G. Valori, P. Démoulin, and K. Dalmasse, A&A **580**, A128 (2015), arXiv:1506.09013 [astro-ph.SR].
[31] A. Brandenburg, Astrophys. J. **901**, 18 (2020), arXiv:2006.12984 [astro-ph.HE].
[32] D. Biskamp, *Nonlinear Magnetohydrodynamics*, Cambridge Monographs on Plasma Physics (Cambridge University Press, 1997).
[33] S. B. Treiman, R. Jackiw, B. Zumino, and E. Witten, *Current Algebra and Anomalies* (Princeton University Press, 1985).
[34] K. Kamada, N. Yamamoto, and D.-L. Yang, Progress in Particle and Nuclear Physics **129**, 104016 (2023).
[35] I. Rogachevskii, O. Ruchayskiy, A. Boyarsky, J. Fröhlich, N. Kleeorin, A. Brandenburg, and J. Schober, apj **846**, 153 (2017), arXiv:1705.00378 [physics.plasm-ph].
[36] A. Vilenkin, Phys. Rev. D **22**, 3080 (1980).
[37] P. J. Feibelman, Phys. Rev. D **4**, 1589 (1971).
[38] M. A. Alpar, S. A. Langer, and J. A. Sauls, Astrophys. J. **282**, 533 (1984).
[39] J. A. Pons and U. Geppert, A&A **470**, 303 (2007), arXiv:astro-ph/0703267 [astro-ph].
[40] J. A. Pons, C. Dehman, and D. Viganò, arXiv e-prints , arXiv:2509.06699 (2025), arXiv:2509.06699 [astro-ph.HE].
[41] A. Kostenko and C. Thompson, The Astrophysical Journal **869**, 44 (2018).
[42] C. Thompson and A. Kostenko, The Astrophysical Journal **904**, 184 (2020).
[43] L. D. Landau and E. M. Lifshits, *Quantum Mechanics: Non-Relativistic Theory*, Course of Theoretical Physics, Vol. v.3 (Butterworth-Heinemann, Oxford, 1991).
[44] V. A. Miransky and I. A. Shovkovy, Phys. Rep. **576**, 1 (2015), arXiv:1503.00732 [hep-ph].
[45] D. E. Kharzeev, L. D. McLerran, and H. J. Warringa, Nuclear Physics A **803**, 227 (2008).
[46] N. P. Armitage, E. J. Mele, and A. Vishwanath, Reviews of Modern Physics **90**, 015001 (2018), arXiv:1705.01111 [cond-mat.str-el].
[47] C. Dehman, D. Viganò, J. A. Pons, and N. Rea, MNRAS **518**, 1222 (2023), arXiv:2209.12920 [astro-ph.HE].
[48] S. Ascenzi, D. Viganò, C. Dehman, J. A. Pons, N. Rea, and R. Perna, arXiv e-prints , arXiv:2401.15711 (2024), arXiv:2401.15711 [astro-ph.HE].
[49] A. Y. Potekhin, J. A. Pons, and D. Page, Space Science Reviews **191**, 239 (2015).
[50] J. M. Pearson, N. Chamel, A. Y. Potekhin, A. F. Fantina, C. Ducoin, A. K. Dutta, and S. Goriely, Monthly Notices of the Royal Astronomical Society **481**, 2994 (2018), https://academic.oup.com/mnras/article-pdf/481/3/2994/25817956/sty2413.pdf.
[51] R. Raynaud, J. Guilet, H.-T. Janka, and T. Gastine, Science Advances **6**, eaay2732 (2020), arXiv:2003.06662 [astro-ph.HE].
[52] R. Durrer and C. Caprini, JCAP **2003**, 010 (2003).
[53] P. Esposito, N. Rea, A. Borghese, F. C. Zelati, D. Viganò, G. L. Israel, A. Tiengo, A. Ridolfi, A. Possenti, M. Burgay, D. Götz, F. Pintore, L. Stella, C. Dehman, M. Ronchi, S. Campana, A. Garcia-Garcia, V. Graber, S. Mereghetti, R. Perna, G. A. R. Castillo, R. Turolla, and S. Zane, The Astrophysical Journal Letters **896**, L30 (2020).
[54] C. Dehman, J. A. Pons, D. Viganò, and N. Rea, MNRAS **520**, L42 (2023), arXiv:2301.02261 [astro-ph.HE].
[55] J. Schober, I. Rogachevskii, and A. Brandenburg, Phys. Rev. Lett. **128**, 065002 (2022), arXiv:2107.12945 [physics.plasm-ph].
[56] J. Schober, I. Rogachevskii, and A. Brandenburg, Phys. Rev. D **105**, 043507 (2022), arXiv:2107.13028 [physics.plasm-ph].
[57] S. Chandrasekhar and P. C. Kendall, Astrophys. J. **126**, 457 (1957).
[58] F. Krause and K.-H. Rädler, *Oxford: Pergamon Press, 1980* (Pergamon Press, Oxford, 1980).